

# A Statistical Approach for Automatic Detection of Ocean Disturbance Features From SAR Images

D. Chaudhuri, A. Samal, A. Agrawal, Sanjay, A. Mishra, V. Gohri, and R. C. Agarwal

**Abstract**—Extraction of features from images has been a goal of researchers since the early days of remote sensing. This paper presents a statistical approach to detect dark curvilinear features due to ocean disturbances caused by wind, movements of surface or underwater objects, and oil spill from SAR images. The image is first enhanced to emphasize the dark curvilinear features using a statistical approach. Then, the curvilinear features are segmented using an iterative approach. The holes in the segmented image are then filled using a recursive scanning method. The image is thinned and unwanted branches are removed using a graph-theory-based technique. Finally, an efficient linking algorithm based on geometric properties is proposed to detect the disturbance features. Our algorithm is evaluated using on both synthetic images with by various levels of added Gaussian noise and on actual SAR images from ERS-2, SEASAT, ENVISAT, and RADARSAT. The results of our approach is compared with those from existing approaches. Results show that, in comparison with the algorithms in literature, our algorithm is more accurate in extracting the features both in terms of the area and shape. In addition, our algorithm runs significantly faster.

**Index Terms**—Adaptive threshold, enhancement, graph theory, remote sensing, segmentation, synthetic aperture radar (SAR).

## I. INTRODUCTION

SATELLITE-BASED synthetic aperture radar (SAR) sensors have proven to be effective in capturing dynamic ocean features including internal waves, currents, eddies, fronts, and the presence of bathymetric features. These features are typically associated with a variable surface current which modulates the sea surface roughness resulting in backscattered radar power [5]. The high resolution of available SAR sensors makes it possible to detect details of these small-scale processes more frequently than other methods. A SAR system will only image surface effects on the ocean as microwave sensors do not penetrate into ocean to any significant depth. Therefore, internal wave characteristics can only be derived from their surface manifestations. The most significant of the surface effects is the modulation of the surface current due to the passage of the internal wave [5].

Large nonlinear internal waves in the ocean induce surface currents and buoyancy. They can have significant impact on

Manuscript received July 21, 2011; revised December 02, 2011; accepted January 08, 2012. Date of publication June 01, 2012; date of current version July 20, 2012.

The authors are with the IAC, DEAL, Raipur Road, Dehradun-248001, Uttarakhand, India, and also with the Department of Computer Science and Engineering, University of Nebraska-Lincoln, Lincoln, NE 68588 USA (corresponding author, e-mail: samal@cse.unl.edu).

Color versions of one or more of the figures in this paper are available online at <http://ieeexplore.ieee.org>.

Digital Object Identifier 10.1109/JSTARS.2012.2186630

ship and submarine operations when they move through a region. Therefore, their detection is important in both civil and military applications. Satellite imagery, especially using SAR, can provide significant clues about the trough and crest patterns of internal waves.

The potential of using satellite imagery for studying oceanic internal waves have long recognized by the oceanographers and remote-sensing researchers. A large body of literature exists in analysis of internal waves, fronts, eddies, and bathymetric signatures [42]. Surface manifestations of oceanic internal waves have been studied in LANDSAT –1 and –2 data since 1972. A study of the wave characteristics yields considerable insight into the physics of their excitation, propagation, and dissipation [1]. Askari *et al.* [2] have examined the radar signatures and changes in the surface roughness associated with oceanic features in the low grazing angle scattering regime. Fu and Holt [3] presented images of three dynamically different regions in the ocean to demonstrate the variety of mesoscale variability detected by the SEASAT SAR. Gagliardini and Colon [4] made a comparison of thermal fronts detected by ERS SAR and LANDSAT TM satellites, analyzing sun glint, upwelling radiance, and the microwave backscatter from the same region, in summer and in winter. Similarly, Gagliardini and Colon [5] suggested an ocean feature detection technique using microwave backscatter and sun glint observation. A close comparison of LANDSAT-TM and ERS SAR data demonstrates that, over a sun glint region, a high-resolution optical sensor can provide observations of sea surface patterns, related to a number of different ocean dynamic processes, such as internal waves, fronts, and eddies, and to bathymetric signatures, which are very similar to those imaged by SAR [5]. Johannessen *et al.* [6] suggested that SAR image expressions of upper ocean circulation features and wind fronts can be distinguished and classified.

Dark formations can be located manually by cropping a border area containing the dark formation or an image window with fixed size can be used, in which threshold algorithms—adapted or not—can be applied. Simple thresholds have one value for the whole image e.g., the half of the average normalized radar cross section (NRCS) of the image [16] or NRSC minus the standard deviation [17]. In adaptive algorithms, threshold is calculated locally, mainly on areas covered by a moving window. In Solberg *et al.* [18], the threshold is set  $k$  dB below the mean value of the moving window, and it is calculated using a multiscale pyramid approach and a clustering step. In Karathanassi *et al.* [19], the threshold is fully adaptive to local contrast and brightness of large image segments, therefore the image window does not have a fixed size, but it varies according to brightness and contrast values of large areas in the image. Del Frate *et al.* [20] used an edge-detection

technique based on image histograms which were derived from areas with suspicious dark formations. Kanaa *et al.* [21] applied a hysteresis thresholding [22] where linear dark formations were successfully detected. Huang *et al.* [23] applied a partial differential equation (PDE)-based level set technique, which represents the slick surface as in implicit propagation interface.

All of the above studies use statistical-based techniques to locate dark formations. A different approach is given by Liu *et al.* [24], Wu and Liu [25] were the use of wavelets for oil spill detection was described. This study was performed for ocean detection on SAR data including oil spills. In latter studies [26], [27], wavelets were used specific for the oil spill detection problem. Moreover, in Benelli and Garzelli [28], dark formations were detected using fractal dimension estimation [43], where a multiresolution algorithm based on fractal geometry for texture analysis was applied. Later, Marghany *et al.* [29], [44] presented a method for modification of the formula of the fractal box counting dimension. A different technique, based on texture analysis, was presented by Marghany [30], [31], where several textures (i.e., entropy, homogeneity, contrast, energy, and correlation) were examined to detect dark formations. In Topouzelis *et al.* [32], an investigation of neural network capabilities and constraints to successfully detect dark formations using high resolution SAR images was performed. Recently, Marghany and Hashim found that neural network has higher performance than Mahalanobis classification for oil spill detection in SAR data [45].

Chen *et al.* [7] proposed a new algorithm to detect typical ocean features such as internal waves, the oceanfront, the ocean eddies and the wind waves in the SAR images with two-dimensional continuous wavelet. A number of researchers have explored the use of Radon transforms to extract features from SAR images. Chen *et al.* [8] proposed an approach for internal wave detection and parameter estimation in SAR ocean image. Chen *et al.* [9] also proposed a linear feature detection method using a gliding window approach. Copeland *et al.* [10] and Zilman *et al.* [11] have proposed techniques approach to the detect ship wakes based on linear feature detection. The main drawback with Radon transform-based approaches for linear feature detection is that they have difficulty detecting line segments which are significantly shorter than the image dimensions since the intensity integration is performed over the entire length of the image [10], [12]. In addition, they have no capability to identify the location of the endpoints of these shorter line segments. Furthermore, linear features that span across the entire image but display some curvature may not produce suitable peaks or troughs in the transform domain. Due to inherent speckle noise, SAR images continuous line segments may be broken into shorter segments which will pose challenges for approaches that use Radon transform. The problem is even more significant when the transform is applied to an image with a high level of noise. Finally, using Radon transform for the detection of dark curvilinear ocean disturbance features is computationally complex.

Pollution from oil spills in the ocean is important in the environmental protection domain. Oil spills caused by intentional or accidental emission have significant impact on wildlife and marine ecosystem. Radar backscatter values from oil spills are very similar to backscatter values from calm sea

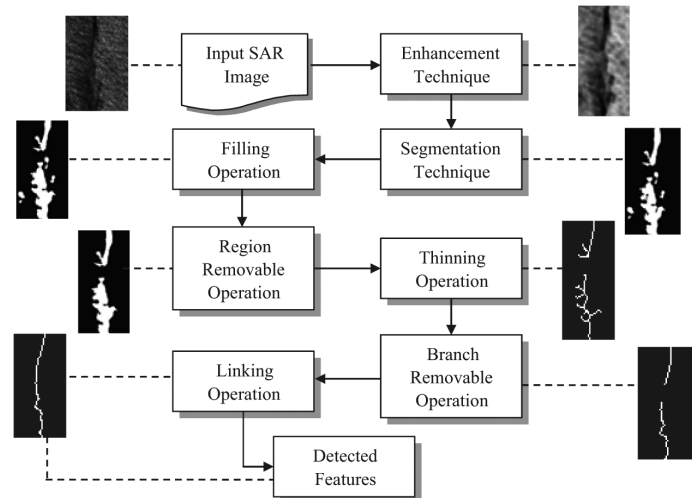


Fig. 1. Schematic of the proposed algorithm.

and other ocean phenomena named *look-alikes* (e.g., currents, eddies, sea surface objects, and underwater objects movement). Topouzelis [13] presented an overview of the methodologies used to detect oil spills on the radar images. Chang *et al.* [14] proposed a fast region-based method for the detection of oil spills in SAR images using a closed-form solution. Chaudhuri *et al.* [15] have presented a two-step approach for highlighting dark curvilinear disturbance features on the ocean surface using statistical approach.

In this paper, we propose a statistical approach to detect dark curvilinear disturbance features on the ocean surface. The main contributions in the proposed method are: 1) local statistical-based enhancement technique to enhance the curvilinear disturbance features on the ocean surface; 2) an efficient segmentation technique based on features occurrence convergence criteria, which partitions the enhanced image into target (ocean disturbance features) and non-target (background) regions; and 3) a graph theory-based approach to accurately aggregate disjoint linear segments into curvilinear features. The proposed technique is compared with other algorithms in literature: 1) Chen *et al.* [9]; 2) Chen *et al.* [7]; 3) Kanaa *et al.* [21]; and 4) Chang *et al.* [14] algorithms. The algorithm is evaluated using both synthetic images with varying levels of Gaussian noise and noise in the different SAR sensors images of ERS-2, SEASAT, ENVISAT and RADARSAT. Results demonstrate that our approach is effective in extracting dark curvilinear disturbance features from the ocean surface. Furthermore, our proposed algorithm is significantly faster than those proposed in literature.

## II. DARK CURVILINEAR FEATURES EXTRACTION ALGORITHM

The focus of this paper is the detection of dark curvilinear features on the ocean surface. Our approach is designed to effectively extract the features using a seven step process as shown in Fig. 1.

- 1) *Image Enhancement:* In this step, the dark curvilinear features are enhanced using a statistical based filtering technique.
- 2) *Segmentation:* Adaptive threshold based segmentation is proposed for isolating dark curvilinear features from the background.

- 3) *Hole Filling*: Many segmented regions have holes due to noise. These holes are filled using a recursive scanning method.
- 4) *Region Removal*: In this step, many regions which do not correspond to our target features are removed.
- 5) *Thinning*: The remaining regions are thinned to derive their one dimensional representation.
- 6) *Spur Removal*: Unwanted spurs that are common in any thinning operation are removed to obtain more clear curvilinear segments using a graph theory based approach.
- 7) *Segment Linking*: Finally, the curvilinear segments are linked together to detect the disturbance features.

The details of the steps are given below.

#### A. Enhancement of Dark Features

The main purpose of enhancement is to improve the contrast of the dark curvilinear features in order to facilitate their downstream recognition. SAR image enhancement techniques can be categorized as: 1) enhancement of spatial features by depressed background information; 2) topographic and geomorphic enhancements for structural and terrain mapping; and 3) texture enhancement related to soil texture and moisture for surface material identification [46]. Our proposed enhancement technique falls in the first category.

Schmitt *et al.* [33] proposed an approach for SAR image de-noising, structure enhancement, and change detection based on the curvelet transformation. The curvelet representation is very redundant that increases the data volume by the factor 16 resulting in greater memory requirements [33]. Murphy *et al.* [12] suggested an approach to the problem of linear feature detection based on the Radon transform.

SAR images suffer from an inherent type of noise, known as *speckle*, which can only be reduced at the by lowering the image resolution. SAR image analysts have therefore been motivated to develop image-processing algorithms which are robust for noisy images. A suitable enhancement operator will decrease the magnitudes of the dark regions by significant amounts, but have less impact on intermediate values. Thus, dark curvilinear features in the original image should be preserved in the filtered image, but with decreased average intensity; here, we present a statistical-based filtering technique for highlighting such dark curvilinear features.

Our approach is motivated by the observation that the dark curvilinear features are both darker and more homogeneous than the background. Since speckle noise, which is brighter than the ocean background, is inherent to all SAR images, it is critical to simultaneously enhance the dark features and reduce the speckle noise effect. Therefore, we focus on those intensity values that contribute for the homogeneity. We compute this homogeneous gray value set in Step 3 of the algorithm below. Replacing the pixel with the minimum of this set not only enhances the dark regions, but also maintains a greater level of homogeneity. Other operators such as maximum, mean, median, or mode will not be able to maintain the homogeneity of the structures, especially at the boundary of the regions while reducing the effect of speckles. This technique is a robust version of the min gray value of the window since it ignores the most extreme values. After adjusting the pixel values in the image, we propose using a high-boost filter to maintain the edge information of the dark

curvilinear features to facilitate their segmentation. We have compared our enhancement results with existing methods in Section III.

---

#### Procedure SARFiltering()

---

{

for each pixel in the image do {

1.  $W = \text{window}(n, n)$ ; // a moving window of size  $n \times n$
2. Calculate *mean gray value* ( $\mu$ ) and *standard deviation* ( $\sigma$ ) for  $W$ .
3. Find the homogeneous gray value set ( $A$ ) with respect to  $\mu$  and  $\sigma$  as defined below:

$$A = \{f : \mu - \sigma \leq f \leq \mu + \sigma, \forall f \in W\}$$

4. Find the minimum value ( $m$ ) of all the gray levels in  $A$ .

$$m = \min(A).$$

5. Replace the current pixel by the minimum,  $m$ .

}

Apply a high-boost filter to preserve the edges;

Apply a contrast stretching technique;

}

The details of the high-boost filter are given here.

Step 1) Consider a  $3 \times 3$  window with weights as follows:

9	19	9
19	137	19
9	19	9

Step 2) Blur the original image ( $f(x, y)$ ) with the above mask and get blur image ( $\bar{f}(x, y)$ )

Step 3) Compute the new image using the following equation for high-boost filter.

$$g(x, y) = (1 + k)f(x, y) - k\bar{f}(x, y) \text{ where } k = 1.5$$

The proposed technique can be categorized as an adaptive filter. It is based on the local statistics within a moving window. The statistics depend on the image characteristics within the window. In comparison, adaptive filtering uses the standard deviation of those pixels within a local box surrounding each pixel to calculate a new pixel value.

It should be noted that the window size will impact the quality of the result. Here we are interested in enhanced curvilinear features, which represent a disturbed area over the ocean surface. The width of these curvilinear features is generally small. Therefore, the size of the window should also be small in the proposed enhancement technique. A large window size may result in many nontarget pixels to be considered for computation of local statistic at the border of the curvilinear (target) features. The enhancement will consequently suffer from too

much nontarget pixels at the border of the curvilinear features. A small window, in contrast, implies increased computational cost. Therefore, the choice of window size does play an important role in the quality of the enhancement. For our research, we found a window size of  $11 \times 11$  to be optimal.

### B. Segmentation

Segmentation is the process of partitioning an image into distinct regions such that each region is homogeneous but the union of two adjacent regions is not. We use segmentation to derive the regions that correspond to the curvilinear features. As described earlier, a number of segmentation algorithms are available in literature [13], [34]–[36], but no single algorithm has proven effective for images acquired from different sensors. Moreover, algorithms developed for one class of image (say ordinary intensity image) does not always work effectively in other classes of images (e.g., magnetic resonance imaging). Therefore, it is often advantageous to either adapt exist segmentation algorithms for specific domains or develop new ones. In this paper, we propose a new technique to segment our targets (dark curvilinear features) in homogenous background (ocean) using a threshold-based technique.

When the targets and background in the image are well contrasted, thresholding with a suitable value can result in effective segmentation. Therefore, the selection of the threshold value is critical. A number of methods for selection of threshold are available in literature [13], [34], [37]. In our algorithm, we use the approached proposed by Otsu [38] as a part of our segmentation. The algorithm chooses the intensity value that maximizes a measure of class separability computed as the ratio of the between class variance to the local variance.

The dark curvilinear features with homogeneous background in SAR images appear darker than the background in the original image. However, after enhancement, these features become even darker. Furthermore, these features occupy significantly less area than in the image. We call this particular observation as *feature occurrence*. The basic idea of the algorithm is to apply Otsu's algorithm iteratively for a set of pixels in the image to minimize the number of regions in the dark region of the image. By computing the *relative frequency* of a particular region based on the automatic threshold value and feature occurrence criteria. The convergence criterion of the proposed automatic threshold based segmentation technique is on the basis of *relative frequency value*. Some mathematical definitions used in our segmentation algorithm, are described below.

**Definition 1:** *Left region*,  $R_l$ , is the set of gray values which are less than or equal to a threshold value  $t$ .  $R_l(t) = \{g : g \leq t, \forall g \in I\}$ , where  $I$  is the set of all pixel values in the image.

**Definition 2:** *Right region*,  $R_r$ , is the set of gray values which are greater than to a threshold value  $t$ .  $R_r(t) = \{g : g > t, \forall g \in I\}$ , where  $I$  is the set of all pixel values in the image.

**Definition 3:** *Left frequency*  $f_l$ : Let  $R_l(t)$  be the left region for a given threshold value  $t$  and  $g \in R_l$  be a gray value. Let the corresponding frequency of  $g$  be  $h_g^l$ . The left frequency is denoted as  $f_l$  and defined by  $f_l = \sum_{g \in R_l} h_g^l$ .

**Definition 4:** *Right frequency*  $f_r$ : Let  $R_r(t)$  be the right region for a given threshold value  $t$  and  $g \in R_r$  be a gray value. Corresponding frequency of  $g$  be  $h_g^r$ . The right frequency is denoted as  $f_r$  and defined by  $f_r = \sum_{g \in R_r} h_g^r$ .

**Definition 5:** *Relative frequency*,  $f_v$  is defined as the ratio of the left frequency to total frequency,  $f_t = f_l + f_r$ .  $f_v = f_l / f_t$ .

Without any loss of generality, let us assume that the size of the image is an integer multiplier ( $>1$ ) of 256. If the size of the image is less than or equal to 256 then the proposed segmentation algorithm is applied for whole image. Otherwise, the proposed segmentation algorithm is applied for each quadrant of size  $256 \times 256$  of the image and finally by merging all segmented results of all quadrants we get the final segmented result. Note that we consider relative frequency for the left region of an image because we are primarily focused on features that are darker and the challenge is to find the right threshold that will accurately segment them. So, in each iteration, we focus only on adjusting the threshold to refine the left region. The segmentation procedure is given below and a schematic is shown in Fig. 2.

#### Procedure Segmentation(I: Image) {

##### 1. // Initialization

```

 $\nu = 0$ ; // number of iterations
 $t^\nu = 256$  // threshold value for 8-bit data
 $f_r^\nu = 0$ ; // right frequency
 $f_l^\nu = n \times n$ ; // left frequency
 $f_c^\nu = n \times n$ ; // current frequency
 $f_v^\nu = 1$ ; // relative frequency
 $R_l^\nu = I$ ; // I is the whole image

```

##### 2. repeat

- a.  $\nu = \nu + 1$
- b.  $t^\nu = \text{OtsuThreshold}(R_l^{\nu-1})$ .
- c.  $f_v^\nu = \text{ComputeRelativeFrequency}(t^\nu)$ ; // Using Definitions 1–5.
- d.  $\Delta f_v^\nu = |f_v^\nu - f_v^{\nu-1}|$ .
- e. if  $f_v^\nu < f_v^{\nu-1}$  OR  $\Delta f_v^\nu > \varepsilon$   
 $\text{ComputeLeftRegion}(t^\nu)$  // Using Definition 1  
until  $(f_v^\nu > f_v^{\nu-1}$  OR  $(\Delta f_v^\nu \leq \varepsilon)$ ;

##### 3. Segment the image using a threshold $t_{\nu-1}$ .

$$g(i, j) = \begin{cases} 1 & \text{if } f(i, j) \leq t^{\nu-1} \\ 0 & \text{if } f(i, j) > t^{\nu-1} \end{cases}$$

where  $I$  and  $S$  are the Input and Segmented images, respectively.

}

The area of the left region (the dark curvilinear features are included in this part) reduces in each iteration. Eventually, this value reaches a minimum which corresponds to the optimal threshold value. Thus, our termination criteria consists of two conditions: 1) when the change relative frequency changes sign (increases after decreasing), i.e.,  $f_v^\eta > f_v^{\eta-1}$  and 2) when the change relative frequency in two consecutive iterations is small, i.e.,  $\Delta f_v^\eta < \varepsilon$  ( $\varepsilon$  is very small). If any one of the two conditions in Step 2(e) is satisfied, then the left region becomes the maximum occupying target region and we do not need to iterate further. The algorithm has only one parameter ( $\varepsilon$ ) and in practice it should be very relatively small. From our experiments, a value

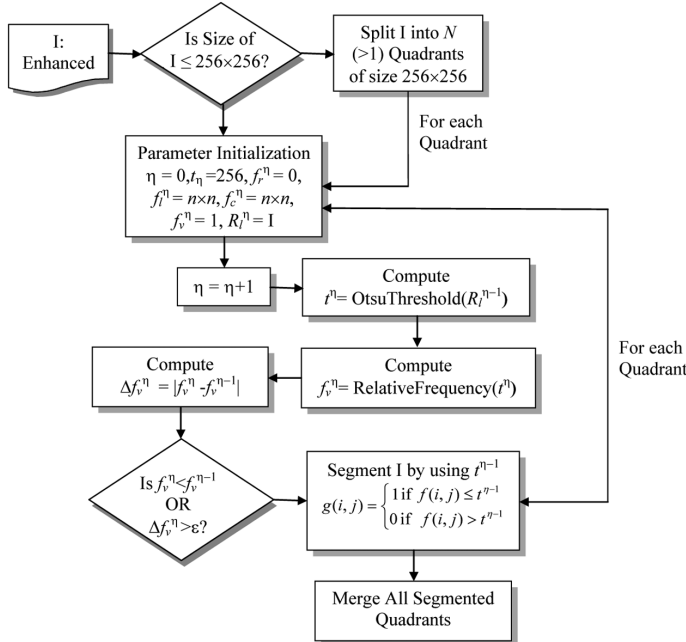


Fig. 2. Flowchart of the segmented procedure.

of  $\leq 10^{-5}$  for  $\epsilon$  works well. The performance of our segmentation algorithm is compared with existing methods in Section III.

### C. Hole Filling

The regions identified after segmentation are in closed form. However, many of them have holes in them due to the uneven nature of the brightness values in the dark regions. Noise is also a contributing factor in some cases as well. These holes must be filled before additional processing like thinning is performed. Many researchers [39], [40] addressed the problem by using morphological operators. We have proposed a specialized recursive-scanning algorithm that is fast and efficient for this application.

After segmentation the foreground (target) pixels are labeled 1 and the background pixels (nontarget) are labeled 0. We begin by selecting a pixel with label 0 and label it as *marked* (say 2). The procedure simultaneously looks for all other pixels in its  $3 \times 3$  neighborhood and labels them as *marked* if they are also nontarget (0) pixels. Once the pixel is *marked*, it is not considered any further. Therefore, this procedure is very fast. When all the nontarget (background) pixels are *marked* the procedure will terminate.

After marking every nontarget pixel (marked as 2), we compute the area of each non-target region and if the area of the non-target region is greater than *area\_threshold* then that non-target region is converted to background (0). Otherwise, the non-target region is converted to target (1).

Unlike many other growing methods, this method is independent of a starting point, and there is no requirement to select suitable properties for including points in the various regions during the growing process, except to check for nontarget pixels (0). This is a variation of region growing method, but growing and marking take place in all directions within a  $3 \times 3$  window simultaneously.

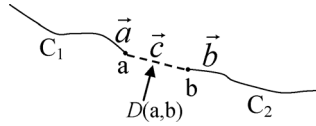


Fig. 3. Linking procedure.

### D. Thinning

After segmentation, many small regions remain due to noise. These regions do not have any physical meaning and are removed using a simple filtering based on the area. Thus, all regions whose area is less than a predefined threshold are removed from further consideration.

During this process, and sometimes during segmentation, a large region breaks up into multiple smaller regions. These regions need to be reconnected using a linking process. Linking is more accurate when connecting linear structures than areal structures since it is difficult to make connectivity decisions based on many end pixels of regions. Therefore, we use a thinning step to derive the linear representation of the regions. In our implementation, we have used a well-known thinning algorithm [41].

### E. Unwanted Branch Removal

Many small disturbance features are associated with the main track of disturbance due to noise, wind, oil spill, sea surface, and underwater objects motion. These minor processes manifest in small branches in the thinned image. To accurately determine the main disturbances, these small unwanted branches must be removed. Using an 8-neighborhood, we classify all of the foreground pixels into *leaf*, *intermediate* or *junction* nodes. Pixels with one, two, and three or more foreground (1) neighbors are called leaf, intermediate and junction nodes, respectively. We identify the lengths of different segments in the thinned image by following pixels from the leaf nodes via intermediate nodes to the junction nodes. Branches that are shorter than some threshold are removed.

### F. Linking Method

At this stage, we have a set of curvilinear feature segments, and, in many cases, an instance of a feature is broken into multiple segments. In the final step, we link them together based on proximity and orientation. We examine the ends of the curvilinear segments and examine if they need to be connected to make a larger segment. To determine if the orientations of the segments are compatible, we examine the consistency in orientation of the segments at multiple locations (see Fig. 3).  $C_1$  and  $C_2$  are two curvilinear feature segments in Fig. 3. Let  $a$  and  $b$  are two end points of  $C_1$  and  $C_2$ , respectively. The orientation of these two curvilinear feature segments at the end points are  $\vec{a}$  and  $\vec{b}$ , respectively. The orientation and distance between the two end points are  $\vec{c}$  and  $D(a,b)$ , respectively. We connect the two segments iff the following conditions are met [47]:

- 1) angle between  $\vec{a}$  and  $-\vec{b}$  is small;
- 2) angle between  $\vec{a}$  and  $\vec{c}$  is small;
- 3) angle between  $\vec{c}$  and  $-\vec{b}$  is small;
- 4) distance between the two pixels is small, i.e.,  $D(a, b) < \epsilon$ .

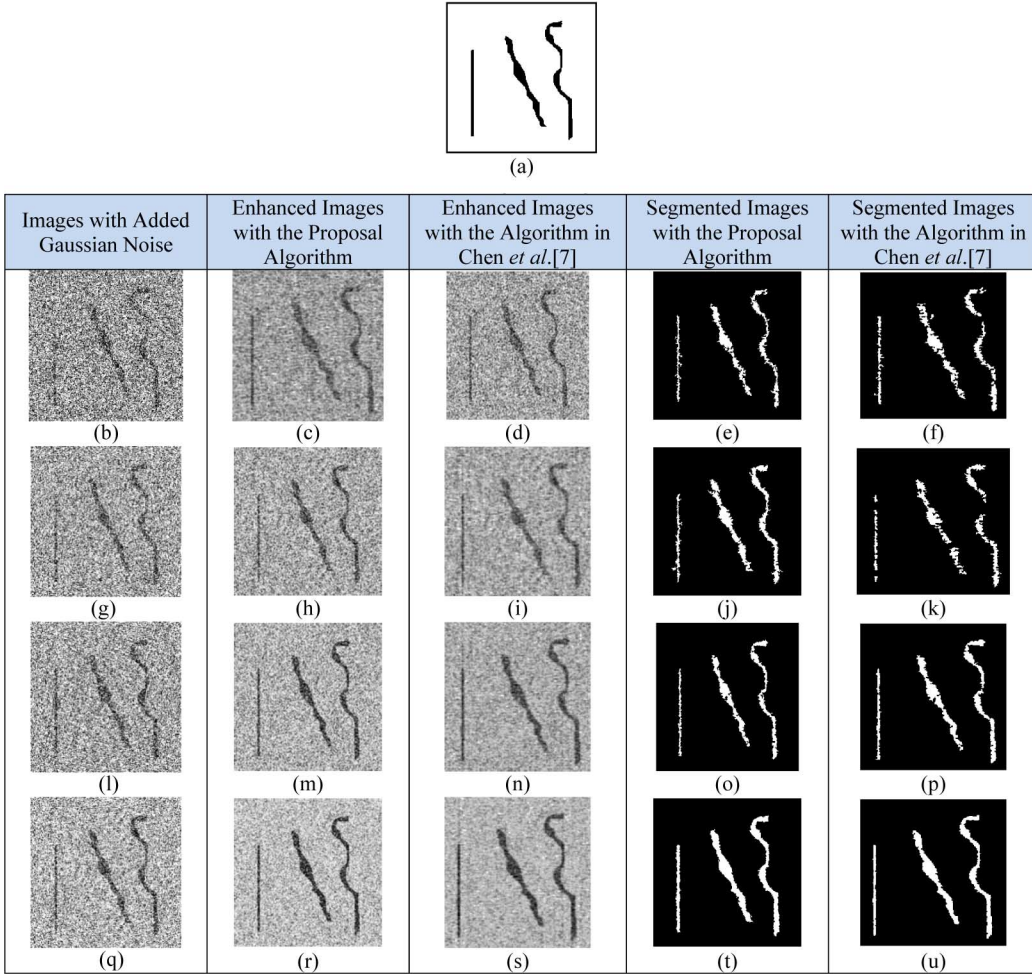


Fig. 4. Synthetic test image of size  $256 \times 256$  and the performance of the proposed algorithm and the algorithm proposed by Chen *et al.* [7].

### III. EXPERIMENTAL RESULTS AND DISCUSSION

To test the effectiveness of the approach, we have used: 1) synthetic test images with different noise levels and 2) real images from a variety of satellites including ERS—2, SEASAT, ENVISAT and RADARSAT. For all of the experiments, the parameter values are fixed as follows: the thresholds  $\varepsilon = 10^{-5}$ ,  $A^T = 50$ , angles of linking =  $15^\circ$ ,  $\Gamma = 1.0$ , and  $L^T = 25$ . Since enhancement and segmentation modules play the most significant role in the algorithm, we have also compared their performance with other well-known techniques [7], [9], [14]. The window size for the enhancement technique is  $11 \times 11$  for all images.

#### A. Synthetic Images

Fig. 4 shows the original synthetic image of size  $256 \times 256$  and the image with different levels of Gaussian noise are added. These noisy images are enhanced and then segmented using the proposed enhancement and segmentation techniques. Fig. 4(a) shows the original image with three different curvilinear features. Images with different levels of Gaussian noise added and their corresponding enhanced image and the segmented images. We compare the results of the proposed algorithm in this paper with the algorithm proposed by Chen *et al.* [7]. It can be seen that the algorithm proposed in this paper demonstrates superior

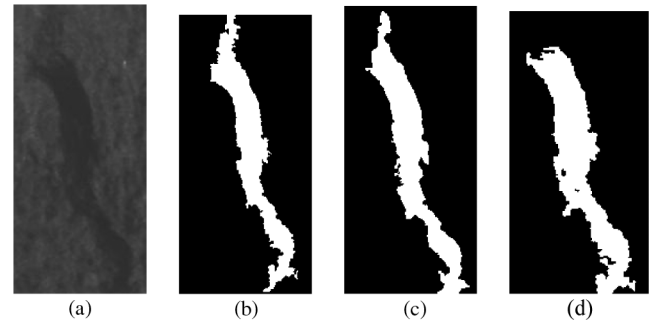


Fig. 5. Performance of feature extraction algorithms using a real ERS-2 SAR image of size  $123 \times 253$ . (a) Original SAR image. (b) Baseline feature (manually derived). (c) Feature derived using the proposed approach. (d) Feature derived using the approach in [14].

performance in both enhancement and the final segmentation. The proposed algorithm identifies the features almost perfectly, even in the presence of significant levels of noise. In contrast, the algorithm by Chen *et al.* [7] is unable to detect the all features properly as shown in Fig. 4(f), 4(k), and 4(p).

#### B. Real Satellite Images

*ERS Images:* Fig. 5(a) shows an original ERS—2 SAR image acquired on 2 December, 1999, near the Kaoshiung Harbor,

TABLE I  
ANALYTICAL COMPARISON BETWEEN THE PROPOSED METHOD AND METHOD PROPOSED BY CHANG *et al.* [14]

Comparison	$A_1$	$A_2$	$A\_Error\ (%)$	$N$	$N_1$	$N_2$	$SP\_Error\ (%)$
Figs. 5(b) and 5(c)	6077	5994	1.36	5458	619	536	21.16
Figs. 5(b) and 5(d)	6077	6097	0.33	4761	1316	1336	55.70
Figs. 6(b) and 6(c)	1954	1899	2.81	1687	267	212	28.39
Figs. 6(b) and 6(d)	1954	1588	18.73	1452	502	136	43.94

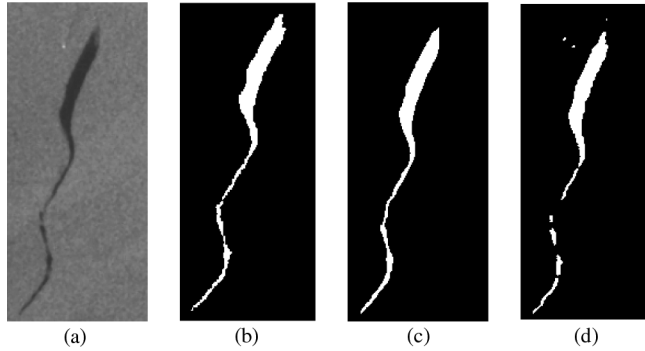


Fig. 6. Performance of feature extraction algorithms using a second real ERS-2 SAR image of size  $122 \times 254$ . (a) Original SAR image. (b) Baseline feature (manually derived). (c) Feature derived using the proposed approach. (d) Feature derived using the approach in [14].

Taiwan, one day after an oil spill (Panama oil tanker occurred near  $N22^{\circ}40' E120^{\circ}05'$  on 1 December, 1999). Our goal here was to detect the dark curvilinear features on the ocean surface. While the focus of this paper is not the detection of oil spills, we use this image to compare the performance the algorithm proposed by Chang *et al.* [14]. To compare the performance of the two algorithms accurately, we use a manually segmented image [Fig. 5(b)] as the baseline. Fig. 5(c) and (d) shows the results of feature extraction using the algorithm proposed in this paper and the algorithm described by Chang *et al.* [14], respectively. A qualitative analysis of the results shows that the proposed algorithm (enhancement and segmentation techniques) extracted the feature more closely to the human judgment.

Fig. 6(a) shows another original ERS-2 SAR image acquired on 15 July, 1999, that contains a long and approximately linear oil spill (dark curvilinear feature). The results of manual feature extraction, the proposed approach and the algorithm given by Chang *et al.* [14], are shown in Fig. 6(b)-(d), respectively. Again, the proposed technique yields results closer to the human expert.

For the scene in Fig. 5(a), the result given by our algorithm is structurally more similar to the baseline than the result from Chang *et al.* [14]. The feature derived using our algorithm, shown in Fig. 5(c), is continuous from the top of the image to the bottom. The feature derived using the algorithm described in [14] [Fig. 5(d)], while continuous, is missing a large area at the top of the image. Furthermore, the result shown in Fig. 5(d) has several holes in the feature, while the feature derived by our algorithm does not. The results of using our algorithm for the image shown in Fig. 6(a) shows that our algorithm is more faithful in reproducing the feature traced by the human expert, given in Fig. 6(b). In sharp contrast to our result, shown in Fig. 6(c), the result from Chang *et al.* [14], shown in Fig. 6(d), shows the feature broken up into a number of smaller segments.

To compare the results of the algorithms analytically, we have introduced two types of errors. It should be noted that the dark formations in SAR images are characterized by their positions and shapes. The two types of errors are given here.

- $A\_Error$  measures the error in the area of the derived feature in comparison to the baseline area and is defined as follows:

$$A\_Error = \frac{|A_1 - A_2|}{A_1} \times 100$$

where  $A_1$  is the actual area derived from the baseline results using an experienced human expert and  $A_2$  is defined as the area of the feature as derived an automated approach [14].

- $SP\_Error$  measures distortion in the shape of the derived features and is defined as follows:

$$SP\_Error = \frac{N_1 + N_2}{N} \times 100$$

where  $N_1$  is the number of points that match in the feature of the baseline image and extracted feature,  $N_2$  is the number points in the actual feature that are missing in the extracted feature, and  $N$  is the number of points in the extracted feature that do not exist in the actual feature. The value of  $N$  is computed by comparing the pixels of the baseline image and extracted feature image and finding the number of pixels which are in both. Let  $B$  be the base line feature set and  $E$  be the extracted feature set. Then,  $N$ ,  $N_1$ , and  $N_2$  can be formally defined as follows;

$$N_1 = \#(B \cap \bar{E}), N_2 = \#(\bar{B} \cap E) \text{ and } N = \#(B \cap E)$$

where  $\bar{A}$  is the complement set of  $A$ .

Table I summarizes the performance of the proposed algorithms and the algorithm proposed by Chang *et al.* [14] using the two images shown in Figs. 4 and 5. Thus, the result by the proposed technique for detection of dark curvilinear feature is consistently more accurate than the algorithm presented in Chang *et al.* [14].

Overall, the area error for our algorithm is 2.85%, and the shape error is 24.78%. In comparison, the corresponding rates for the algorithm proposed in [14] are 9.53% and 49.82%. Thus, our algorithm is more accurate in identifying the features.

*SEASAT Images:* In Fig. 7(a), a  $256 \times 256$  pixel SEASAT SAR image of a sea region containing a ship wake in the typical "V" pattern is shown. Fig. 7(b) shows the enhanced image by the proposed enhancement technique and at the same time the enhanced image as by Chen *et al.* [7] algorithm is shown in Fig. 7(c). Also, the detected features by the proposed segmentation technique and by Chen *et al.* [7] algorithm are shown

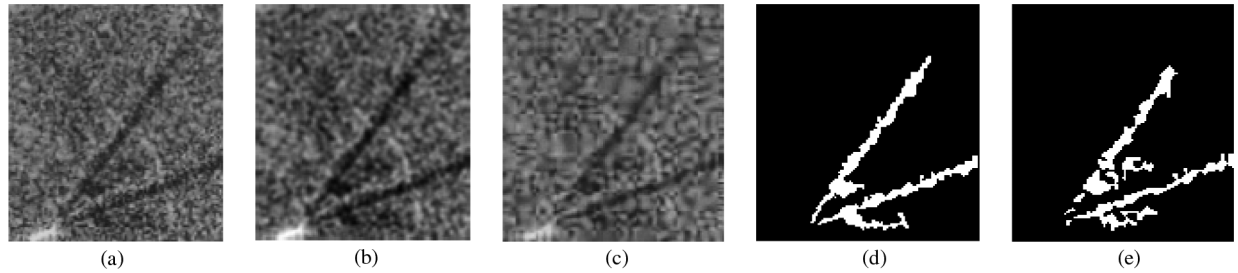


Fig. 7. Comparison of algorithms using an original SEASAT SAR image of size  $256 \times 256$ . (a) Original SEASAT SAR image. (b) Enhanced with proposed algorithm. (c) Enhanced with algorithm in [7]. (d) Extracted features with our approach. (e) Extracted features using [7].

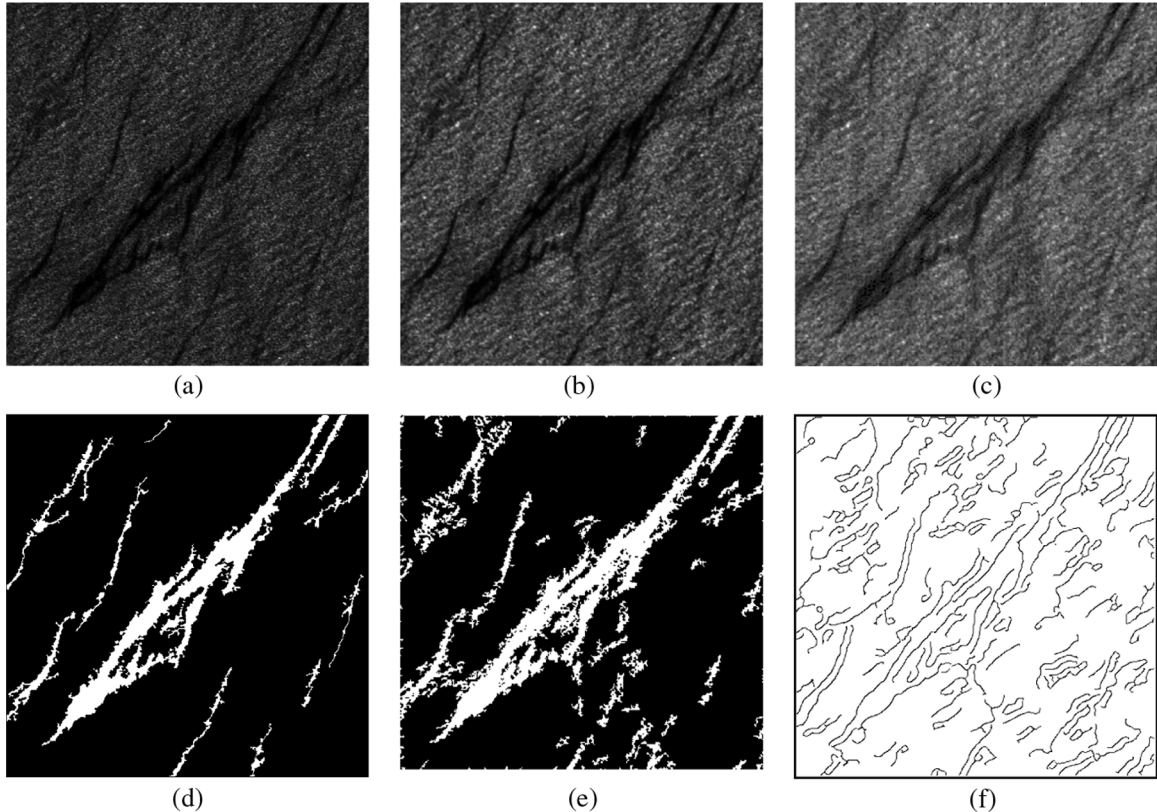


Fig. 8. Comparison of algorithms using an original ENVISAT SAR image of size  $512 \times 512$ . (a) Original SAR image. (b) Enhanced with proposed algorithm. (c) Enhanced with the algorithm of Chen *et al.* [9]. (d) Detected features from (b) by the proposed technique; (e) Detected features from image (c) by the algorithm of Chen *et al.* [9]. (f) Detected features using the algorithm by Kanaa *et al.* [21].

in Fig. 7(d) and (e), respectively. The results show that the proposed enhancement and segmentation techniques are better than those of the algorithm by Chen *et al.* [7] as per dark features detection is a concern.

**ENVISAT Images:** Another ENVISAT SAR image is considered for comparison result with other methods. An original ENVISAT SAR image of size  $512 \times 512$  is shown in Fig. 8(a). The enhanced image and detected features by the proposed enhancement and segmentation techniques are shown in Fig. 8(b) and (d), respectively. At the same time, the enhanced image and the detected features by Chen *et al.* [9] algorithm are shown in Fig. 8(c) and (e), respectively. The detected features are quite smooth and better than the results given by the algorithm by Chen *et al.* [9]. In the whole aspect, the results show that the proposed enhanced and segmentation techniques are better than the algorithm by Chen *et al.* [9]. Fig. 8(f) shows

the detected features achieved using the algorithm developed by Kanaa *et al.* [21] [applied a hysteresis thresholding (Canny [22], using the thresholds standard deviation ( $\sigma$ ), lower and upper thresholds are 4.2, 0.3 and 0.9, respectively)]. We have detected the features with various combinations of standard deviation ( $\sigma$ ), lower and upper thresholds, and Fig. 8(f) is better than any other combinationss. Still, many false alarms are detected by the algorithm by Kanaa *et al.* [21] and the detected features by the proposed technique are better than those using the algorithm of Kanaa *et al.* [21].

We now briefly analyze the various steps in the proposed algorithm using an ENVISAT SAR image of size  $512 \times 512$  shown in Fig. 9(a). It is evident from the image that the curvilinear features of interest are darker than the homogeneous background with speckle noise. Fig. 9(b) shows the segmented image of the original image by Otsu's method [38] without

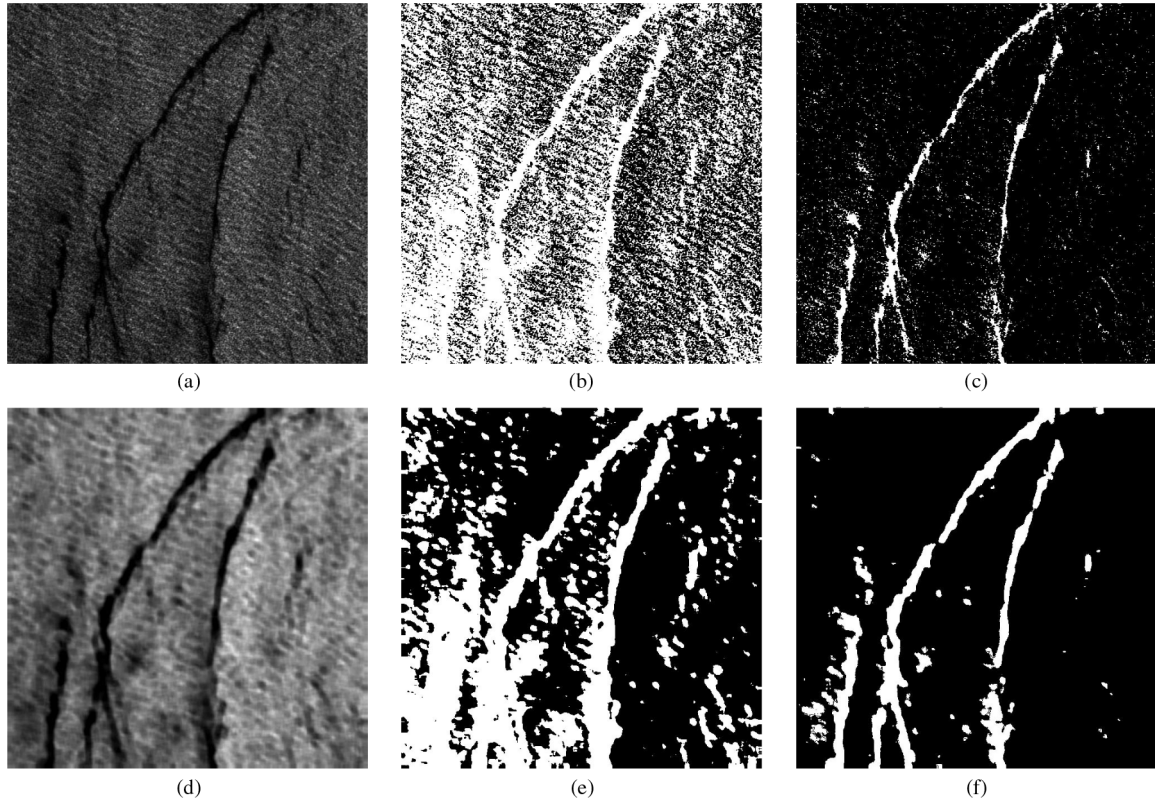


Fig. 9. Comparison of segmentation results using an ENVISAT SAR image of size  $512 \times 512$ . (a) Original ENVISAT SAR image. (b) Segmentation of original image using single threshold. (c) Segmentation of original image using the proposed segmentation technique. (d) Features enhanced image. (e) Segmentation of enhanced image using a single threshold. (f) Segmentation of enhanced image using proposed technique.

feature occurrence convergence criteria and the computed threshold value is  $Th = 56$ . Due to presence of noise and same type signatures as the target feature signatures, many segmented regions are obtained. Thus, it is difficult to isolate the main target features from the background. Result after using our proposed segmentation algorithm of the original image is shown in Fig. 9(c). Many small segmented regions still remain due to noise. In addition, the main dark curvilinear features are discontinuous and by area removal technique these small target feature regions may be deleted. Consequently, it became a problem to link two adjacent target features as the intermediate distance between these two adjacent regions is greater than the threshold. It is noticed that the segmented result of the original image by the proposed segmentation technique [Fig. 9(c)] is better than the segmented result of the original image by using a single threshold [Fig. 9(b)].

Fig. 9 also shows the results of the segmentation approaches using the enhanced image. Fig. 9(d) shows the enhanced version of the image shown in Fig. 9(a). It is clear that the target features are more prominent in the enhanced image. Fig. 9(e) shows the segmentation of the enhanced image using Otsu's method [38] of selection threshold without feature occurrence convergence criteria and the computed threshold value is  $Th = 28$ . While the result in Fig. 9(e) is better than Fig. 9(b), many nontarget features still remain. Also, it is difficult to isolate the target features from the background in many places. Finally, the result of segmentation of the enhanced image using our proposed algorithm is shown in Fig. 9(f). It can be seen from Fig. 9(f) that small-unwanted regions are not present and also the regions in

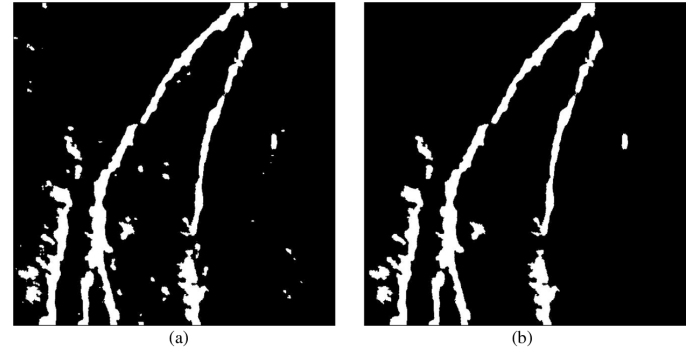


Fig. 10. Some postprocessing steps after segmentation. (a) Image after hole filling. (b) Image after area filtering.

particular dark curvilinear features are better connected and isolated from the background than the previous segmented results. Thus, the results show that our proposed algorithm using the enhancement approach results in superior segmentation.

A close look at the segmentation results [Fig. 9(f)] shows that many holes appear within the closed form segmented regions. The presence of these holes will negatively impact the quality of the detected features. Hence, we fill up these holes using a simple hole filling approach as described earlier. The result of filling holes is shown in Fig. 10(a). Finally, we remove the small regions that are not significant in the image. Fig. 10(b) shows the result after area filtering.

Fig. 11 shows the final steps in the feature extraction based on thinning. As described earlier, the thinning operation is re-

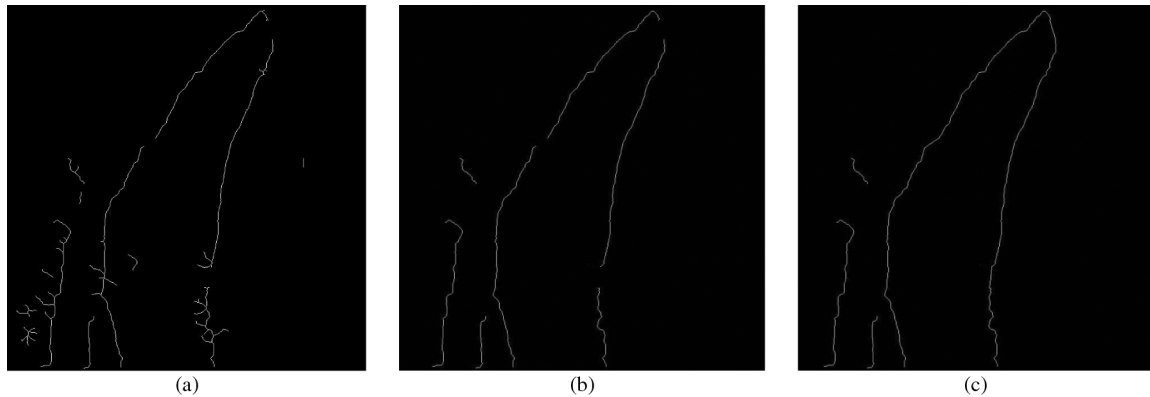


Fig. 11. Steps in thinning and linking liner features to derive the final features. (a) Thinned image. (b) Image after branch removal. (c) Final linked image.

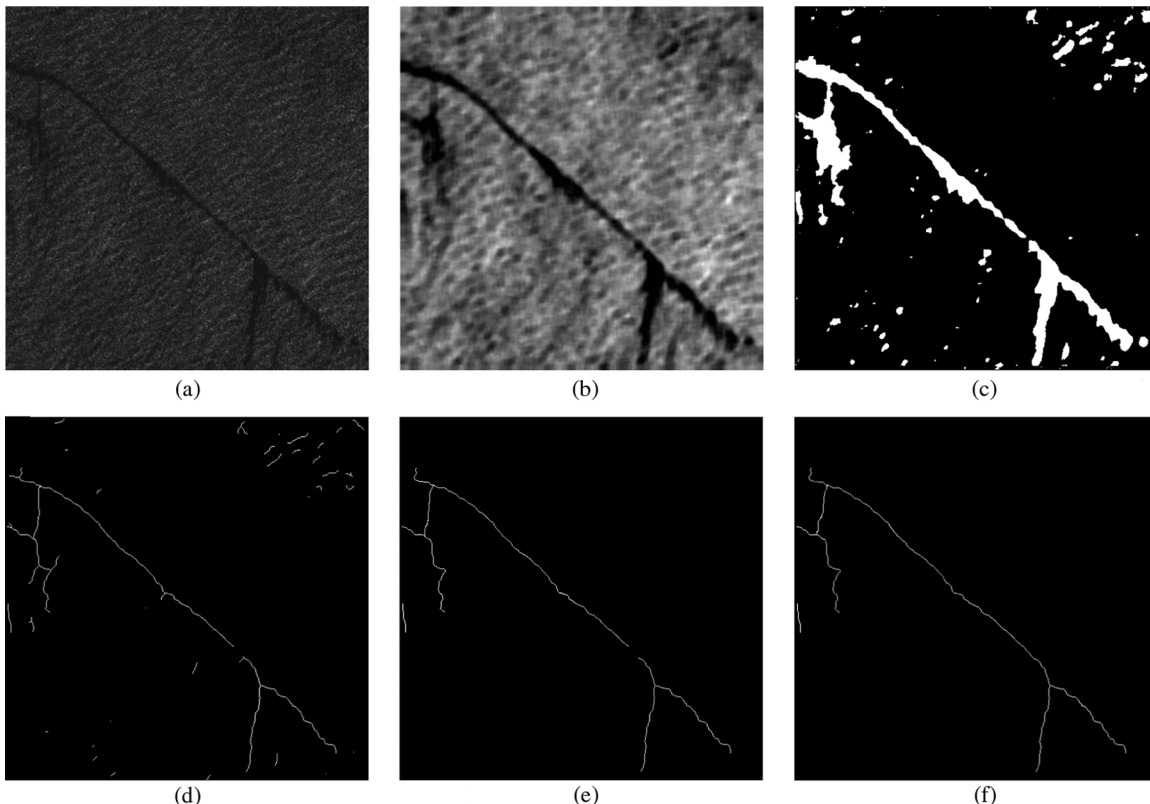


Fig. 12. Steps in feature extraction of curvilinear features from a RADARSAT images. (a) Original RADARSAT image. (b) Features enhanced image. (c) segmented image using proposed algorithm. (d) Thinned image. (e) Image after branch removal. (f) Final linked image.

quired to remove the unwanted branches of the main features as well as to join the curvilinear disjoint features segments. Many small insignificant disturbance features are associated with main track which are removed using the proposed branch removal operation and the branch-removed image. Fig. 11(a) shows the thinned image derived from Fig. 10(b). Fig. 11(b) shows the image after the branch removal step and Fig. 11(c) shows the image after the final linking step, which is the final detected dark curvilinear disturbance feature.

*RADARSAT Image:* Fig. 12(a) shows an original RADARSAT SAR image of size  $512 \times 512$ . The enhanced image and the result after segmentation are shown in Fig. 12(b) and (c), respectively. The thinned images after holes filling and area filtering, with branch-removed and linked (which is final detected dark curvilinear feature) images are shown in Fig. 12(d)-(f), respectively.

TABLE II  
COMPARISON OF COMPUTATION SPEED FOR DIFFERENT ALGORITHMS (IN  
MILLISECONDS)

	Proposed Algorithm	Chen <i>et al.</i> [7]	Chang <i>et al.</i> [14]	Chen <i>et al.</i> [9]	Kanaa <i>et al.</i> [21]
Fig 4	422	5191			
Fig 5	282		2341		
Fig 6	188			1562	
Fig 7	324	3895			
Fig 8	719			13158	5321

*Computational Speed:* The time to compute the features is also an important criterion in selecting an algorithm. Table II summarizes the performance of our proposed algorithm to others in literature. All algorithms are implemented and timed on an HPxw6400 workstation (Intel(R) Xeon(R), 5130 @200 GHz, 2.00 GB RAM, Microsoft windows XP). Table II shows

the runtimes for our proposed algorithm and the other algorithms proposed by Chen *et al.* [7], Chang *et al.* [14], Chen *et al.* [9], and Kanaa *et al.* [21] for the different images used in this paper. Table II shows that our proposed algorithm is significantly faster than others proposed in literature.

The proposed algorithm is simple, and the procedure remains reliable even in presence of noise. Also, it is computationally less expensive than many other algorithms. In summary, we have demonstrated that the proposed algorithm is both more accurate and computationally more efficient than other methods.

#### IV. CONCLUSION AND FUTURE RESEARCH DIRECTIONS

Dark formation detection is considered to be a fundamental step in ship wakes, submarine wakes, or oil-spill detection systems. Once dark formations are detected, classification methods can be applied to characterize them. Features are central for classification since they are used as inputs to the classifier. Therefore, the combination of features which discriminate better the ship wakes, submarine wakes or oil spill from the look-alikes is important for classification.

We have presented a statistical-based approach to detect the dark curvilinear (ocean disturbance) features with homogeneous background (ocean) caused due to wind, sea surface objects, or underwater objects movement and oil spill in SAR images. The accuracy of the proposed enhancement and iteration-based segmentation technique has been demonstrated through extensive set of experiments. Our algorithm was applied to both synthetic images with various levels of added Gaussian noise and on actual SAR images from ERS-2, SEASAT, ENVISAT, and RADARSAT. We have also compared the results with other existing methods of enhancement and segmentation for such features. Overall, the accuracy of our algorithms is at least twice that of the algorithms in literature in terms of area and the shape of the features. In addition, our algorithm is at least an order of magnitude faster than the competing algorithms.

Our future work includes the extraction of features from the results we have obtained in this paper and the development of classifiers to identify ship wakes or submarine wakes or oil spills. Improving the detection accuracy of the classifier scheme, multi-hypotheses, which contain oil-polluted, unpolluted sea area, ship wakes or submarine wakes, and look-alikes, and the more useful features of training images for data modeling, will be the main focus of our future study.

#### ACKNOWLEDGMENT

The authors would like to thank Prof. L. Chang, Department of Communications and Guidance Engineering, National Taiwan Ocean University, Taiwan, for his encouragement and for some images used in this research (Figs. 4 and 5).

#### REFERENCES

- [1] J. Appel, H. M. Byrne, J. R. Proni, and R. Sellers, "A study of oceanic internal waves using satellite imagery and ship data," *Remote Sens. Environ.*, vol. 5, pp. 125–135, 1976.
- [2] F. Askari and T. F. Donato, "Detection of oceanic fronts at low grazing angles using an X band real aperture radar," *J. Geophys. Res.*, vol. 101, no. 9, pp. 20,883–20,898, 1996.
- [3] L. L. Fu and B. Holt, "Some examples of detection of oceanic mesoscale eddies by the SEASAT synthetic aperture radar," *J. Geophys. Res.*, vol. 88, no. 3, pp. 1,844–1,852, 1983.
- [4] D. A. Gagliardini and P. C. Colon, "A comparative assessment on the use of SAR and high-resolution optical images in ocean dynamics studies," *Int. J. Remote Sens.*, vol. 25, no. 7–8, pp. 1271–1275, 2004.
- [5] D. A. Gagliardini and P. C. Colon, "Ocean feature detection using microwave backscatter and sun glint observations," *Gayana Supl. TI Proc.*, vol. 68, no. 2, pp. 180–185, 2004.
- [6] J. Johannessen, R. Shuchman, O. Johannessen, and K. Davidson, "Synthetic aperture radar imaging of upper ocean circulation features and wind fronts," *J. Geophys. Res.*, vol. 96, no. 6, pp. 10,411–10,422, 1991.
- [7] J. Chen, J. Sun, and J. Yang, "Typical ocean features detection in SAR images," in *Proc. Int. Workshop Education Technol. Training Int. Workshop Geosci. Remote Sens.*, Shanghai, China, Dec. 21–22, 2008, vol. 2, pp. 425–428.
- [8] B. Chen, J. Chen, and J. Sun, "Internal wave detection and parameter estimation from SAR images based on a novel Radon transform method," in *Proc. Int. Workshop Education Technol. Training Int. Workshop Geosci. Remote Sens.*, Shanghai, China, Dec. 21–22, 2008, vol. 1, pp. 234–237.
- [9] J. Chen, J. Sun, S. Xu, and B. Chen, "Novel radon transform-based method for linear feature detection in open water SAR images," in *Proc. MIPPR*, Y. Wang, J. Li, B. Lei, and J. Yang, Eds., 2007, vol. 6790, p. 67900C.
- [10] A. C. Copeland, G. Ravichandran, and M. M. Trivedi, "Localized radon transform-based detection of ship wakes in SAR images," *IEEE Trans. Geosci. Remote Sens.*, vol. 33, no. 1, pp. 35–45, Jan. 1995.
- [11] G. Zilman, A. Zapolski, and M. Marom, "The speed and beam of a ship from its wake's SAR images," *IEEE Trans. Geosci. Remote Sens.*, vol. 42, no. 10, pp. 2335–2343, Oct. 2004.
- [12] L. M. Murphy, "Linear feature detection and enhancement in noisy image via the Radon transform," *Pattern Recognit. Lett.*, vol. 4, no. 4, pp. 279–284, 1986.
- [13] K. N. Topouzelis, "Oil spill detection by SAR images: Dark formation detection, feature extraction and classification algorithms," *Sensors*, vol. 8, pp. 6642–6659, 2008.
- [14] L. Chang, Z. S. Tang, S. H. Chang, and Y. L. Chang, "A region-based GLRT detection on oil spills in SAR images," *Pattern Recognit. Lett.*, vol. 29, pp. 1915–1923, 2008.
- [15] D. Chaudhuri, A. Mishra, Sanjay, A. Agrawal, and V. Gohri, "Automatic detection of ocean disturbance features from satellite SAR imagery," in *Proc. Symp. Adv. Remote Sens. Technol. Applic. Microw. Remote Sens.*, Ahmedabad, India, Dec. 18–20, 2008, p. 37.
- [16] B. Fiscella, A. Giancaspro, F. Nirchio, and P. Trivero, "Oil spill detection using marine SAR images," *Int. J. Remote Sens.*, vol. 21, pp. 3561–3566, 2000.
- [17] F. Nirchio, M. Sorgente, A. Giancaspro, W. Biamino, E. Parisato, R. Ravera, and P. Trivero, "Automatic detection of oil spills from SAR images," *Int. J. Remote Sens.*, vol. 26, no. 6, pp. 1157–1174, 2005.
- [18] A. Solberg, C. Brekke, and P. O. Husoy, "Oil spill detection in Radarsat and ENVISAT SAR images," *IEEE Trans. Geosci. Remote Sens.*, vol. 45, no. 3, pp. 746–755, Mar. 2007.
- [19] V. Karathanassi, K. N. Topouzelis, P. Pavlakis, and D. Rokos, "An object-oriented methodology to detect oil spills," *Int. J. Remote Sens.*, vol. 27, pp. 5235–5251, 2006.
- [20] F. Del Frate, A. Petrocchi, J. Lichtenegger, and G. Calabresi, "Neural networks for oil spill detection using ERS-SAR data," *IEEE Trans. Geosci. Remote Sens.*, vol. 38, no. 5, pp. 2282–2287, May 2000.
- [21] T. F. N. Kanaa, E. Tonye, G. Mereier, V. P. Onana, J. M. Nagono, P. L. Frison, J. P. Rudant, and R. Garello, "Detection of oil slick signatures in SAR images by fusion of hysteresis thresholding responses," in *Proc. Geosci. Remote Sens. Symp.*, 2003, vol. 4, no. 21, pp. 2750–2752.
- [22] J. Canny, "A computational approach to edge detection," *IEEE Trans. Pattern Anal. Mach. Intell.*, vol. 8, pp. 679–698, 1986.
- [23] B. Huang, H. Li, and X. Huang, "A level set method for oil slick segmentation in SAR images," *Int. J. Remote Sens.*, vol. 26, pp. 1145–1156, 2005.
- [24] A. K. Liu, C. Y. Peng, and S. Y. S. Chang, "Wavelet analysis of satellite images for coastal watch," *IEEE J. Oceanic Eng.*, vol. 22, pp. 9–17, 1997.
- [25] S. Y. Wu and A. K. Liu, "Towards an automated ocean feature detection, extraction and classification scheme for SAR imagery," *Int. J. Remote Sens.*, vol. 24, pp. 935–951, 2003.
- [26] R. Araujo, F. De Medeiros, R. Costa, R. Marques, R. Moreira, and J. Silva, "Locating oil spill in SAR images using wavelets and region growing," *Lecture Note Computer Science*, vol. 3029, pp. 1184–1193, 2004.

- [27] S. Derrode and G. Mercier, "Unsupervised multiscale oil slick segmentation from SAR images using a vector HMC model," *Pattern Recognit.*, vol. 40, pp. 1135–1147, 2007.
- [28] G. Benelli and A. Garzelli, "Oil-spills detection in SAR images by fractal dimension estimation," in *Proc. Int. Geosci. Remote Sens. Symp.*, Hamburg, Germany, 1999, vol. 1, pp. 218–220.
- [29] M. Marghany, M. Hashim, and A. P. Cracknell, *Fractal Dimension Algorithm for Detecting Oil Spills Using RADARSAT-1 SAR*. O. Gervasi and M. Gavrilova, Eds. Berlin, Germany: Springer-Verlag, 2007, vol. 4705, pp. 1054–1062.
- [30] M. Marghany, "RADARSAT automatic algorithms for detecting coastal oil spill pollution," *Int. J. Appl. Earth Obs. Geoinf.*, vol. 3, pp. 191–196, 2001.
- [31] M. Marghany, "RADARSAT for oil spill trajectory model," *Environ. Modell. Softw.*, vol. 19, pp. 473–483, 2004.
- [32] K. N. Topouzelis, V. Karathanassi, P. Pavlakis, and D. Rokos, "Dark formation detection using neural networks," *Int. J. Remote Sens.*, vol. 29, pp. 4705–4720, 2008.
- [33] A. Schmitt, B. Wessel, and A. Roth, "Curvelet approach for SAR image denoising, structure enhancement and change detection," in *Proc. CMRT09, LAPRS*, U. Stilla, F. Rottensteniner, and F. Papadimitriou, Eds., Paris, France, Sep. 3–4, 2009, vol. XXXVIII, part-3/W4.
- [34] N. R. Pal and S. K. Pal, "A review on image segmentation techniques," *Pattern Recognit.*, vol. 16, no. 9, pp. 1277–1294, 1993.
- [35] D. Chaudhuri, A. Mishra, S. K. Anand, and V. Gohri, "Optimal splitting technique for remote sensing satellite imagery data," in *Proc. SPIE*, 2001, vol. 4388, pp. 79–88.
- [36] A. Rekik, M. Zribi, A. B. Hamida, and M. Benjelloun, "Review of satellite image segmentation for optimal fusion system based on the edge and region approaches," *Int. J. Comput. Sci. Network Security*, vol. 7, no. 10, pp. 242–250, 2007.
- [37] R. C. Gonzalez and R. E. Woods, *Digital Image Processing*. Delhi, India: Pearson Education, 2001.
- [38] N. Otsu, "A threshold selection method from gray level histograms," *IEEE Trans. Syst., Man Cybern.*, vol. 9, pp. 62–66, 1979.
- [39] C. R. Giardina and E. R. Daugherty, *Morphological Methods in Image Processing*. Englewood Cliffs, NJ: Prentice-Hall, 1988.
- [40] J. Serra, *Image Analysis and Mathematical Morphology*. New York: Academic Press, 1982.
- [41] A. Rosenfeld and A. Kak, *Digital Picture Processing*. New York: Academic, 1982.
- [42] M. Marghany, M. Hashim, and A. P. Cracknell, "3-D visualizations of coastal bathymetry by utilization of airborne TOPSAR polarized data," *Int. J. Digital Earth*, vol. 3, no. 2, pp. 187–206, 2010.
- [43] M. Marghany, A. Cracknell, and M. Hashim, "Modification of fractal algorithm for oil spill detection from RADARSAT-1 SAR data," *Int. J. Appl. Earth Observation Geoinf.*, vol. 11, pp. 96–102, 2009.
- [44] M. Marghany, A. Cracknell, and M. Hashim, "Modification of fractal algorithm for oil spill detection from RADARSAT-1 SAR data," *Int. J. Appl. Earth Observation Geoinf.*, vol. 11, pp. 96–102, 2009.
- [45] M. Marghany and M. Hashim, "Comparison between Mahalanobis classification and neural network for oil spill detection using RADARSAT-1 SAR data," *Int. J. Phys. Sci.*, vol. 6, no. 3, pp. 566–576, 2011.
- [46] , V. Singhroy, D.D. Nebert, and A. I. Johnson, Eds., "Environmental and geological site characterization in vegetated area: Image enhancement guidelines," in *Remote Sensing and GIS for Site Characterization: Applications and Standards, ASTM STP 1279*. : ASTM, 1996, pp. 5–16.
- [47] A. Mukherjee, S. K. Parui, D. Chaudhuri, B. B. Chaudhuri, and R. Krishnan, "An efficient algorithm for detection of road-like structures in satellite images," in *Proc. IEEE ICPR*, 1996, pp. 875–879.

**D. Chaudhuri** is currently a Scientist with the Defense Electronics Applications Laboratory (DEAL), Dehradun, India. He has authored or coauthored over 45 papers in international journals and conferences in the area of image analysis.

**A. Samal** is a Professor with the Department of Computer Science and Engineering, University of Nebraska-Lincoln. His research interests include image analysis including biometrics, document image analysis, and computer vision applications. He has published extensively in these areas.

**A. Agrawal** is a scientist with the Defense Electronics Applications Laboratory (DEAL), Dehradun, India.

**Sanjay** is a Scientist with the Defense Electronics Applications Laboratory (DEAL), Dehradun, India.

**A. Mishra** is a scientist with the Defense Electronics Applications Laboratory (DEAL), Dehradun, India.

**V. Gohri** retired as Scientist 'G' from the Defense Electronics Applications Laboratory (DEAL), Dehradun, India. He has authored or coauthored 18 papers in international and national journals and conferences.

**R. C. Agarwal** is the director of the Defense Electronics Applications Laboratory (DEAL), Dehradun, India.